Article

Netrin-1-Regulated Distribution of UNC5B and DCC in Live Cells Revealed by TICCS

Angelica A. Gopal,[1,2] Benjamin Rappaz,[2,3] Vincent Rouger,[1] Iain B. Martyn,[3] Peter D. Dahlberg,[3] Rachel J. Meland,[1] Ian V. Beamish,[2,4] Timothy E. Kennedy,[2,4] and Paul W. Wiseman[1,2,3,*]

[1]Department of Chemistry, [2]McGill Program in Neuroengineering, [3]Department of Physics, and [4]Department of Neurology and Neurosurgery, Montreal Neurological Institute, McGill University, Montreal, Quebec, Canada

ABSTRACT Netrins are secreted proteins that direct cell migration and adhesion during development. Netrin-1 binds its receptors deleted in colorectal cancer (DCC) and the UNC5 homologs (UNC5A–D) to activate downstream signaling that ultimately directs cytoskeletal reorganization. To investigate how netrin-1 regulates the dynamic distribution of DCC and UNC5 homologs, we applied fluorescence confocal and total internal reflection fluorescence microscopy, and sliding window temporal image cross correlation spectroscopy, to measure time profiles of the plasma membrane distribution, aggregation state, and interaction fractions of fluorescently tagged netrin receptors expressed in HEK293T cells. Our measurements reveal changes in receptor aggregation that are consistent with netrin-1-induced recruitment of DCC-enhanced green fluorescent protein (EGFP) from intracellular vesicles to the plasma membrane. Netrin-1 also induced colocalization of coexpressed full-length DCC-EGFP with DCC-T-mCherry, a putative DCC dominant negative that replaces the DCC intracellular domain with mCherry, consistent with netrin-1-induced receptor oligomerization, but with no change in aggregation state with time, providing evidence that signaling via the DCC intracellular domain triggers DCC recruitment to the plasma membrane. UNC5B expressed alone was also recruited by netrin-1 to the plasma membrane. Coexpressed DCC and UNC5 homologs are proposed to form a heteromeric netrin-receptor complex to mediate a chemorepellent response. Application of temporal image cross correlation spectroscopy to image series of cells coexpressing UNC5B-mCherry and DCC-EGFP revealed a netrin-1-induced increase in colocalization, with both receptors recruited to the plasma membrane from preexisting clusters, consistent with vesicular recruitment and receptor heterooligomerization. Plasma membrane recruitment of DCC or UNC5B was blocked by application of the netrin-1 VI-V peptide, which fails to activate chemoattraction, or by pharmacological block of Src family kinase signaling, consistent with receptor recruitment requiring netrin-1-activated signaling. Our findings reveal a mechanism activated by netrin-1 that recruits DCC and UNC5B to the plasma membrane.

INTRODUCTION

Netrins are a family of secreted chemotropic guidance cues that direct cell migration and adhesion during development of the nervous system, lung, mammary glands, pancreas, muscle, and vasculature (1). Netrin family members are composed of ~600 amino acids and are members of the laminin superfamily (2).

The netrin receptor deleted in colorectal cancer (DCC) is a single-pass transmembrane protein with an extracellular domain composed of four immunoglobulin (Ig) domains and six fibronectin type III domains (3). Different domains in netrin-1 bind to the fourth and fifth fibronectin domains, with the capacity to cross-link DCC (4,5). The DCC intracellular domain (ICD) includes three conserved sequences termed P1, P2, and P3 (3). Binding to extracellular netrin-1 has been proposed to trigger homodimerization of the intracellular DCC P3 domains to activate signaling mechanisms that ultimately result in cytoskeletal reorganization and mediate chemoattraction (1,4,6).

The UNC5 homologs, UNC5A–D in mammals, are a second family of single-pass transmembrane netrin receptors. Extracellularly, they are composed of two Ig domains and two thrombospondin type I domains, with the Ig domains implicated in netrin-1 binding (5,7). The UNC5 ICD includes a ZU-5 domain, a DCC-binding (DB) motif, and a death domain (7,8). UNC5 homologs are required for chemorepellent responses to netrins, either as part of an UNC5-DCC netrin receptor complex, or in the absence of DCC (1,9,10). Binding of the intracellular DB domain of UNC5 to the P1 domain of DCC is thought to promote UNC5-DCC heterodimerization (9,11). The UNC5-DCC receptor heterodimer is proposed to exhibit increased sensitivity to netrin-1 and thereby facilitate long-range chemorepellent responses, whereas an UNC5 homolog in the absence of DCC is sufficient for short-range chemorepellent responses to higher concentrations of secreted netrin (11). However, even when expressed in the same cell, DCC and an UNC5 homolog may function independently. For example, the *Drosophila* DCC ortholog Frazzled and

Submitted September 21, 2015, and accepted for publication December 21, 2015.

*Correspondence: paul.wiseman@mcgill.ca

Editor: Kalina Hristova.

0006-3495/16/02/0623/12

http://dx.doi.org/10.1016/j.bpj.2015.12.022

UNC5 partition to different cardioblast plasma membrane domains, with one receptor mediating adhesion and the other repulsion, during blood vessel formation (12). The mechanisms regulating the interaction and distribution of DCC and UNC5 homologs, and chemorepulsion in general, remain poorly understood.

N-terminal domains VI and V of netrins are homologous to the N-terminal domains of laminins (13,14). The netrin C-terminal domain exhibits sequence similarity to the tissue inhibitors of metalloproteinase, both of which bind heparin and are rich in basic amino acid residues (13,15,16). A fragment of netrin-1 composed of only domains VI and V, termed netrin VI-V, binds to DCC and UNC5 homologs (3,7). Recombinant monomeric netrin-1 VI-V disrupts the chemoattractant activity of full-length netrin-1, but is sufficient to repel migrating oligodendrocyte precursor cells (17), providing evidence that, unlike chemoattraction, chemorepellent signaling does not require netrin receptor oligomerization; however, how netrin VI-V influences UNC5-DCC interactions and the downstream signaling activated are not known.

Although it is understood that DCC and UNC5 family members can function independently or as a complex to mediate cellular responses to netrin-1, the dynamic contribution of each protein to the regulation of various responses to netrin remains unclear. Netrin receptor trafficking has been studied, revealing DCC recruitment to the plasma membrane via protein kinase A (PKA) activation (18) and protein-kinase-C-triggered endocytosis of UNC5A (19), yet the regulation of receptor trafficking by netrin-1 itself is not well understood.

To study the response of these proteins to netrin-1 in living cells, we employed confocal and total internal reflection fluorescence (TIRF) microscopy to image netrin-1-induced changes in the distribution of fluorescently tagged netrin-1 receptors: full-length DCC with enhanced green fluorescent protein (DCC-EGFP), full-length UNC5B-mCherry, and DCC-T-mCherry, which replaces the DCC ICD with mCherry. The image series were then processed via fluorescence fluctuation analysis.

Fluorescence fluctuation analysis methods have been widely used to measure the dynamics and binding kinetics of macromolecules in cells. The original method, fluorescence correlation spectroscopy, has been used to measure the diffusion of proteins and lipids in cells (20–22), whereas macromolecular interactions have been characterized using the two-color variant, fluorescence cross-correlation spectroscopy (23–26).

Image correlation spectroscopy (ICS) extended the analysis of fluorescence fluctuations to the spatial domain inherently sampled in imaging microscopy. ICS was first applied to single images to measure clustering and receptor distributions in fixed cells (27,28). It was expanded to measure slow and fast macromolecule transport dynamics, using temporal ICS (TICS) (29,30) and raster-scan ICS, respectively (31,32). The two-color extensions, temporal image cross-correlation spectroscopy (TICCS) and spatial ICCS (29,33), also measure colocalization. Analogous imaging fluorescence correlation spectroscopy variants were introduced based on TIRF microscopy and have been applied to cellular systems (34,35), and photobleaching ICS has been used to measure the aggregate distribution of Aβ proteins in nerve cells (36).

Full generalization to space and time correlation analysis was implemented with spatiotemporal ICS (37,38), permitting the measurement of transport maps of flow of cytoskeletal and adhesion-related macromolecules. This, too, was extended to a two-color cross-correlation variant (STICCS) to map interactions and cotransport of integrins and paxillin in cell focal adhesions (39). More recently, spatiotemporal ICS was used to generate diffusion maps in cells via calculation of an average mean-square displacement versus time plot in a technique termed iMSD (40).

In this study, we apply TICCS to analyze a sliding window of image frames of variable length to calculate time-dependent changes in the density, degree of aggregation, and colocalization of fluorescently tagged netrin-1 receptors before and after treatment with netrin-1. We report that netrin-1 triggers the translocation of DCC and UNC5B from intracellular vesicles to the plasma membrane, and that plasma membrane DCC and UNC5B colocalize in response to netrin-1. Our findings demonstrate that netrin-1 directs the multimerization of receptors on the plasma membrane and activates intracellular signaling to recruit netrin receptors to the plasma membrane.

MATERIALS AND METHODS

Cell culture

Human embryonic kidney (HEK) 293T cells were cultured in Dulbecco's modified Eagle's medium supplemented with 10% fetal bovine serum, 4 mM L-glutamine, 100 units/mL penicillin, 0.1 mg/mL streptomycin, and 0.1 mM nonessential amino acids (Gibco, Carlsbad, CA). Cells were maintained in a humidified, 5% CO_2 atmosphere at 37°C. Cells were grown for 2 days in 35 mm microwell dishes (MatTek, Ashland, MA) before being imaged. Only cells below passage 25 were used for experiments. At 24 h postplating, plasmids encoding full-length DCC-EGFP and/or full-length UNC5B-mCherry, or full-length DCC-EGFP and DCC-T-mCherry, regulated by the cytomegalovirus promoter, were transfected into the cells using LTX Lipofectamine with the PLUS reagent, as specified by the manufacturer (Life Technologies, Carlsbad, CA). Full-length netrin-1 and truncated netrin-1, containing domains VI and V, were generated and purified as previously described (13,17,41).

Confocal microscopy

Optical section imaging of basal membranes of transfected HEK293T cells was performed using a Zeiss 710 inverted confocal laser scanning microscope (CLSM) (Zeiss, Thornwood, NY) equipped with a 40×/NA 1.2 water immersion objective lens. Cells expressing moderate levels of recombinant protein were imaged.

The EGFP label was excited using the 488 nm line of an argon ion laser and mCherry with a 594 nm line from a HeNe laser. Fluorescence emission from EGFP and mCherry was separated using a main dichroic beam splitter

488/594 and EGFP emission was collected in channel 1 through a 525 ± 35 nm band-pass filter, whereas emission from mCherry was collected in channel 2 through a 605 nm long-pass filter.

Autofluorescence from cells was approximately the same magnitude as the background fluorescence of the medium (shown in Fig. S1 in the Supporting Material, with intensity traces displayed in Fig. S2), which was subtracted from the region of interest in the analysis. Detector cross talk was measured in both channels by exciting cells expressing only EGFP constructs with the 594 nm laser, and cells expressing only mCherry constructs with the 488 nm line. Measured image intensities were no different from background fluorescence intensity levels (displayed in Fig. S3, with intensity traces shown in Fig. S4).

During imaging, cells were maintained at ~37°C in a 5% CO_2 environment in an incubator (Live Cell Instrument, Seoul, South Korea). The cells were allowed to equilibrate in the imaging incubator for at least 10 min before data acquisition to avoid thermal drift.

TIRF microscopy

Imaging of basal membranes of HEK293T cells transfected with DCC-EGFP was performed using a homebuilt TIRF microscope based on an inverted Olympus IX71 microscope (Olympus, Richmond Hill, Ontario, Canada) equipped with a 60×/NA 1.45 oil immersion TIRF objective lens. The EGFP label was excited with an OBIS 488 LS laser (Coherent, Santa Clara, CA). Excitation and emission were separated using an HQFITC U-T41001 filter cube (Olympus). Fluorescence emission was collected on a 1024 × 1024 Andor iXon Ultra 888 EMCCD camera (SnowHouse Solutions, Lac-Beauport, Quebec, Canada). The system was controlled by LabVIEW (National Instruments, Austin, TX).

During imaging, cells were maintained at ~37°C in HEPES-buffered medium (Gibco), with a homebuilt heated box around the microscope. Cells were allowed to equilibrate for at least 10 min before data acquisition to reduce thermal drift.

Live-cell imaging experiments

CLSM image time series of 600 or more frames were taken of the live cells, with sampling at 970 ms/frame, where cells were treated after the 200th frame, thus yielding an initial prestimulation baseline for all measured parameters. TIRF image time series of 1200 or more frames were taken of the live cells, with sampling at 500 ms per frame, where cells were treated after the 500th frame.

For stimulation, 1.6 μg of full-length netrin-1 or netrin VI-V peptide, was injected via a pipette tip or syringe (10 μL, Hamilton, Reno, NV) inserted into the incubator and positioned at the edge of the dish for CLSM experiments. During TIRF experiments, the solution was pipetted directly into the dish. Controls were taken where no treatment occurred, and blank controls substituted an equivalent volume of cell culture medium. For Src family kinase inhibition, PP2 or PP3 were added at a final concentration of 2 μM 15 min before imaging. Controls included addition of PP2 or PP3 without netrin-1 stimulation.

For a 600 frame time series with stimulation occurring at frame 200, frames 1–175 were considered prestimulation, with poststimulation from frame 225 to the end of the measured change (i.e., decrease or increase) in a TICCS-measured variable to quantify the maximum change in time of an experimental parameter. In cases where no change was observed, the poststimulation measurement was identified as frame 225 to the end of the time series.

Image correlation analysis

ICS image analysis software was written using MATLAB R2013a (The MathWorks, Natick, MA) and run on a PC computer with a 3.40 GHz processor and 16 GB of random-access memory.

Theory

The fluorescence fluctuation image analysis methods ICS, TICS, and image cross-correlation spectroscopy (ICCS) have been described earlier (27–30,33,37,42–44). We provide the basic theory of these techniques needed for understanding the results in this article and the extension of TICCS to a sliding time window.

Generalized spatiotemporal correlation function

ICS is based on space and/or time correlation analysis of fluorescence intensity fluctuations sampled in a fluorescence microscopy image series. The fluorescence fluctuations arise from variations in the number of fluorescent molecules in different areas of the image as detected within each sampled focal spot, as well as changes in the number of emitting molecules in time from any fixed focal spot. The image time series can be thought of as a matrix of fluorescence intensity fluctuations in space and time, keeping in mind that for CLSM imaging, the images are recorded by point scanning as the laser beam focus is repeatedly raster-scanned across the sample. Spatial/temporal correlation functions are subsequently calculated from time series of specific regions of interest (ROIs) within the image, and the correlation functions are fit by nonlinear least squares with appropriate model functions to obtain output parameters (see below).

The generalized two-detection-channel (a and b) normalized spatiotemporal intensity fluctuation correlation function of an ROI is defined in Eq. 1 as a function of two orthogonal spatial lag variables, ξ and η (corresponding to lateral pixel shifts along the image spatial dimensions), and a temporal lag variable, τ (corresponding to shifts in time between image frames):

$$r_{ab}(\xi,\eta,\tau) = \frac{\langle \delta i_a(x,y,t)\delta i_b(x+\xi,y+\eta,t+\tau)\rangle}{\langle i_a\rangle_t\langle i_b\rangle_{t+\tau}}, \quad (1)$$

where $\delta i_{a/b}(x,y,t)$ is the intensity fluctuation in a given channel at pixel position (x,y) at time t, defined as $\delta i(x,y,t) = i(x,y,t) - <i(x,y,t)>_t$. The angular brackets in the numerator indicate a spatial correlation function calculated over all pixel fluctuations in pairs of images separated by the time lag, τ. The correlation function is normalized by average intensities of the image ROIs for frames recorded at time t and $t+\tau$, respectively. For each detection channel, we calculate an autocorrelation function (set $b = a$ and $a = b$ in the subscripts), as well as the cross correlation function between detection channels ($a \neq b$).

The generalized formula allows us to consider the special cases of calculations for TICS and TICCS.

TICS

Equation 2 is the discrete approximation of Eq. 1 evaluated at zero spatial lag, giving the temporal intensity fluctuation correlation function averaged over the ROI:

$$r_{ab}(0,0,\Delta t) = \frac{1}{XY}\sum_{x=1}^{X}\sum_{y=1}^{Y}\frac{\delta i_a(x,y,t)\delta i_b(x,y,t+\Delta t)}{\langle i_a(x,y,t)\rangle_t\langle i_b(x,y,t+\Delta t)\rangle_{t+\Delta t}}, \quad (2)$$

where Δt is the discrete analog of the time lag, τ, in units of image frames and X and Y are the number of pixels spanning the ROI horizontally and vertically (45).

For this study involving membrane receptors, the calculated temporal correlation functions are fit to a decay model for 2D diffusion (Eq. 3, and see Fig. 2) where the fit parameters are highlighted in bold:

$$r_{ab}(0,0,\Delta t) = \mathbf{g}_{ab}(\mathbf{0},\mathbf{0},\mathbf{0})\left(1+\frac{\Delta t}{\boldsymbol{\tau}_{\mathbf{d}ab}}\right)^{-1} + \mathbf{g}_{\infty ab}. \quad (3)$$

The output fit parameters are (for detection channel/labeled species x, where $x = a$ or b) $\boldsymbol{g_{xx}(0,0,0)}$, the zero-lags correlation function amplitude; $\boldsymbol{\tau_{dxx}}$, the characteristic diffusion time; and $\boldsymbol{g_{\infty xx}}$, the long-temporal-lag offset, accounting for incomplete decay of the correlation function when immobile or very slowly diffusing species are present. The average number of independent mobile fluorescent particles (e.g., clusters/aggregates) per beam focal spot area is the reciprocal of the correlation function amplitude for single-channel autocorrelation ($x = a$ or b):

$$\langle \mathrm{n_{xx}} \rangle = \frac{1}{\mathrm{g_{xx}}(0,0,0)}. \tag{4}$$

The diffusion coefficient of species x is calculated from the characteristic diffusion time and the e^{-2} focal spot radius, ω_{oxx}:

$$\mathrm{D_{xx}} = \frac{\omega_{oxx}^2}{4\tau_{dxx}}, \tag{5}$$

whereas the fraction of immobile species is calculated as

$$\mathrm{f_{immobile,\,\mathit{x}}} = \frac{\mathrm{g_{\infty xx}}}{\mathrm{g_{\infty xx}} + \mathrm{g_{xx}}(0,0,0)}. \tag{6}$$

The mean number of independent mobile fluorescent particles can be converted to the cluster density (CD_{xx}) using Eq. 7, which is an area density of the independent clusters. The degree of aggregation (DA_{xx}) is calculated as the ratio of the average intensity to the cluster density (Eq. 8) and is related to the mean and variance of the distribution of aggregate size for a clustered system, assuming that the average intensity for the ROI is proportional to the mean number of fluorescent subunits per beam area independent of how they are distributed or clustered in the imaged particles (28).

$$CD_{xx} = \frac{\langle n_{xx} \rangle}{\pi \omega_{0xx}^2} \tag{7}$$

$$DA_{xx} = \frac{\langle i \rangle_{xx}}{CD_{xx}} \tag{8}$$

TICCS

To measure colocalization, TICCS is applied using Eqs. 2 and 3, but with cross correlation between the two detection channels ($a \neq b$). The average number of colocalized particles in the beam area, $<n_{ab}>$, is calculated using the amplitudes of the cross correlation function normalized by the amplitudes of the autocorrelation functions, and the ratio of the effective areas is defined by the focal spots of the two lasers ($A_b > A_a = \pi {\omega_{oaa}}^2$) (24):

$$\langle n_{ab} \rangle = \frac{\mathbf{g_{ab}}(\mathbf{0},\mathbf{0},\mathbf{0})}{\mathbf{g_{aa}}(\mathbf{0},\mathbf{0},\mathbf{0}).\mathbf{g_{bb}}(\mathbf{0},\mathbf{0},\mathbf{0})} \frac{A_b}{A_a}. \tag{9}$$

The area ratio is included to account for the difference in size of the two excitation and detection volumes and was determined from the fitted beam radii from spatial correlation functions calculated for each channel and corroborated experimentally with beads. We calculate the interaction fractions M1 and M2, which are ratios of the number of colocalized particles to the number of particles for each channel. The two interaction fractions are defined in Eqs. 10 and 11, where M1 refers to the fraction of mCherry particles interacting with EGFP particles, and M2 refers to the fraction of EGFP particles interacting with mCherry particles (a = EGFP, b = mCherry):

$$M1 = \frac{\mathbf{g_{ab}}(\mathbf{0},\mathbf{0},\mathbf{0}) + \mathbf{g_{\infty ab}}}{\mathbf{g_{aa}}(\mathbf{0},\mathbf{0},\mathbf{0}) + \mathbf{g_{\infty aa}}} = \frac{\langle n_{ab} \rangle}{\langle n_{bb} \rangle}, \tag{10}$$

$$M2 = \frac{\mathbf{g_{ab}}(\mathbf{0},\mathbf{0},\mathbf{0}) + \mathbf{g_{\infty ab}}}{\mathbf{g_{bb}}(\mathbf{0},\mathbf{0},\mathbf{0}) + \mathbf{g_{\infty bb}}} = \frac{\langle n_{ab} \rangle}{\langle n_{aa} \rangle}. \tag{11}$$

Sliding-window TICCS

To resolve the time-dependent changes of TICCS output variables over a long image time series, a sliding time window version of TICCS was applied. For a time series with N images, a window size of W images and a max time lag of Δt is chosen. Within the time series, there are $N - W + 1$ windows, with the first window starting at image 1 and the last window at $N - W + 1$. Inside each window, TICCS is implemented $W - \Delta t + 1$ times from the first image of the window to the $W - \Delta t + 1$ image of the window. Each of the $W - \Delta t + 1$ calculated variables (such as the interaction fraction) determined from the TICCS analyses are then averaged to give one set of mean variables for that window. Applying the procedure to all overlapping windows in the time series yields the variable as a function of time, where one window is relative to its neighbors. All analyses here have been implemented with $W = 200$ and $\Delta t = 100$, so that a sufficient number of time points are used for the calculation of the correlation functions, with an adequate number of TICCS analyses per window.

RESULTS

To examine the effect of netrin-1 stimulation on the cell-surface distribution of UNC5B and DCC, four different combinations of expressed receptors were imaged and analyzed by TICCS: cells expressing DCC-EGFP, UNC5B-mCherry, DCC-EGFP/UNC5B-mCherry, and DCC-EGFP/DCC-T-mCherry. Fig. 1 shows a typical set of CLSM images taken from a DCC-EGFP/UNC5B-mCherry experiment. DCC-EGFP/UNC5B-mCherry expressing cells were also treated with the Src family kinase inhibitor PP2 or its inactive analog PP3 (46) in addition to full-length netrin-1 and the netrin VI-V peptide (17).

We calculated the correlation functions for the ROIs shown in Fig. 1 and fit them to the 2D diffusion model (Eq. 3).These results are shown in Fig. 2. We calculated an average of 25 DCC-EGFP units/μm^2, with a diffusion coefficient of 0.04 μm^2/min and an immobile fraction of 0.38. In the UNC5B-mCherry channel, we detected an average of 33 units/μm^2, with a diffusion coefficient of 0.03 μm^2/min and an immobile fraction of 0.41. We detected 4 mobile co-localized units/μm^2, with a diffusion coefficient of 0.04 μm^2/min. The M1 and M2 interaction fractions, including the immobile population, are calculated to be 0.58 and 0.51 respectively.

Although our initial aim was to image receptors localized to the plasma membrane, the low diffusion coefficients of the receptors suggested that these populations of DCC and UNC5B might be localized to clusters of receptors in the plasma membrane or, perhaps more likely, present in intracellular vesicles tethered under the plasma membrane that are within the confocal volume. The diffusion coefficients

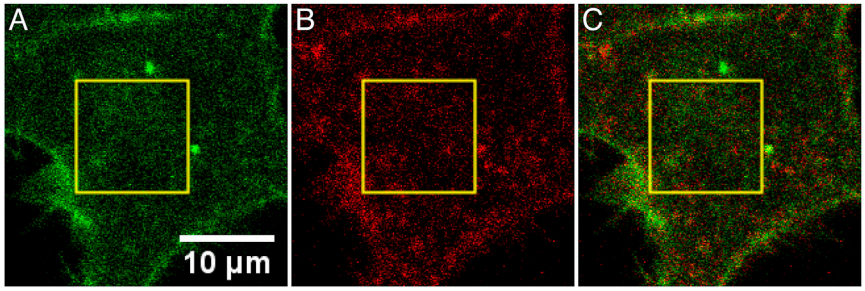

FIGURE 1 CLSM images of HEK293T cells expressing recombinant DCC-EGFP and UNC5B-mCherry before netrin-1 stimulation. (*A*) Channel 1: EGFP channel showing distribution of DCC. (*B*) Channel 2: mCherry channel showing UNC5B distribution. (*C*) Composite overlay image of (*A*) and (*B*). The yellow box shows a typical ROI selected for TICCS analysis. To see this figure in color, go online.

of these populations did not change significantly upon netrin-1 treatment.

Netrin-1 recruits DCC to the plasma membrane

To investigate the effect of netrin-1 on the distribution of each full-length receptor, we imaged HEK293T cells expressing only DCC-EGFP or UNC5B-mCherry by CLSM and performed sliding-window TICCS analysis on the resulting image series (Fig. 3).

When stimulated with netrin-1, the average cluster density of DCC-EGFP increased by 12%, whereas the degree of receptor aggregation decreased by 11% and the mean intensity remained constant. Although the decrease in aggregation state after netrin-1 stimulation may seem paradoxical, these findings are consistent with the interpretation that a population of DCC is localized to membrane proximal intracellular vesicles that are recruited to the plasma membrane as a result of netrin-1 application, assuming that the receptors in the plasma membrane are less clustered compared to those stored in compact vesicles within the confocal volume.

To address the possibility that netrin-1 recruits DCC to the plasma membrane, DCC-EGFP was expressed in HEK293T cells and imaged via TIRF microscopy (Fig. 4), which limits excitation to a much narrower focal volume proximal to the cell membrane relative to confocal microscopy. The increased intensity detected between Fig. 4, *A* and *B*, reveals an increase in DCC-EGFP at the basal membrane induced by netrin-1 stimulation. Fig. 4 *C* illustrates the formation of filapodia and lamellopodia enriched with DCC, consistent with previous studies quantifying increased filopodia formation and membrane extension evoked by DCC activation in HEK293T cells (47). Intensity traces quantifying the increase in membrane associated DCC are shown in Fig. 4 *D*.

Sliding-window TICCS was then performed on the TIRF microscopy image series (Fig. 5), revealing two responses to netrin-1: netrin-1 response 1 (R1) and netrin-1 response 2 (R2), differentiated by the change in cluster density. In netrin-1 R1, the average cluster density increased by ~400%, whereas in netrin-1 R2, the average cluster density decreased by ~70%. The degree of aggregation increased in both cases: in R1 by 20,000% and in R2 by 12,000%, and the mean intensity increased by ~40% in R1 and R2.

The netrin-1-induced increase in intensity for both responses supports the conclusion that DCC is recruited by netrin-1 from intracellular vesicles to the plasma membrane. Furthermore, the increase in aggregation indicates that netrin-1 oligomerizes DCC upon application. The R1 response shows a considerable increase in DCC cluster density, consistent with DCC recruitment to the plasma membrane that results in an increase in cluster density and degree of aggregation. In contrast, the R2 response exhibits a decrease in DCC cluster density, suggesting that significant aggregation of plasma membrane DCC dominates over DCC recruitment, as shown in Fig. 4.

To independently address whether application of netrin-1 recruits DCC to the plasma membrane, recombinant DCC-EGFP was expressed in HEK293T cells. Proteins exposed on the extracellular face of the plasma membrane were then selectively labeled by cell-surface biotinylation. The biotinylated proteins were isolated using streptavidin-coated beads and assessed by Western blot analysis for DCC. Increased biotinylated cell-surface DCC was detected 5 min after exposure to netrin-1 (Fig. S5), supporting the

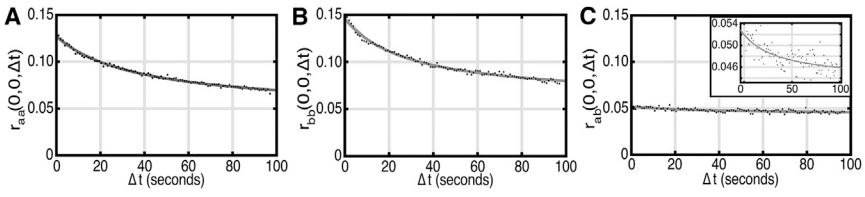

FIGURE 2 Representative TICCS correlation functions and fits to the 2D diffusion model (Eq. 3) calculated for the ROIs shown in Fig. 1. (*A*) Autocorrelation function and best fit for channel 1 DCC-EGFP. (*B*) Autocorrelation function and best fit for channel 2 UNC5B-mCherry. (*C*) Cross-correlation function and best fit for channel 1 × 2, with the inset showing a zoomed scale to show the decay and fit. $R^2 = 0.99$ for the autocorrelation functions and 0.51 for the cross-correlation function. The correlation-function data are the discrete points and the solid lines are the best fits. $\Delta t = 0.97$ s.

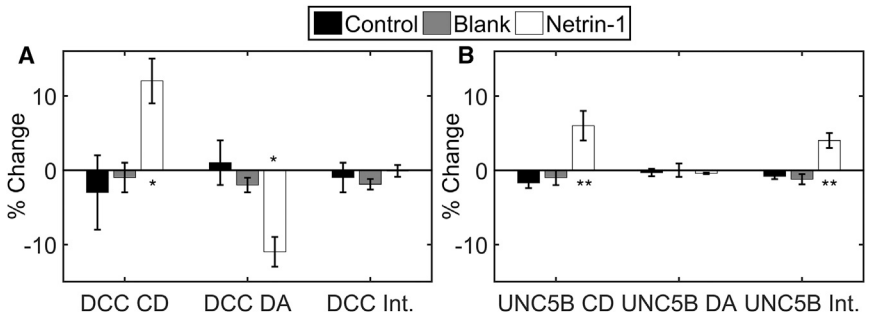

FIGURE 3 Mean percentage changes in cluster density (CD), degree of aggregation (DA), and average intensity (Int.) of (*A*) transfected DCC-EGFP HEK293T cells and (*B*) transfected UNC5B-mCherry HEK293T cells in the control, blank, and netrin-1 stimulation conditions. Error bars indicate the mean ± SE; $*p < 0.05$ and $**p < 0.001$ compared to control and blank stimulation, evaluated by one-way analysis of variance (ANOVA); significance was evaluated at a 90% confidence level (CL) (*) and a 95% CL (**) via the two-tailed *t*-test. $N = 5–9$.

conclusion that DCC is rapidly recruited to the plasma membrane after stimulation with netrin-1.

Netrin-1 recruits UNC5B to the plasma membrane

Application of netrin-1 to UNC5B-mCherry HEK293T-expressing cells resulted in an increase in the average cluster density by 6%; the average intensity increased by 4%, whereas the degree of aggregation did not change. This suggests a relatively modest recruitment of UNC5B from outside of the sampled volume, possibly also from intracellular vesicles to the plasma membrane, but in an aggregation state not different from preexisting UNC5B.

Netrin-1 oligomerizes DCC in the absence of an intracellular domain

We then co-expressed full-length DCC-EGFP with DCC-T-mCherry, which replaces the DCC ICD with mCherry to assess the contribution of activated DCC signaling. A significant difference in colocalization was detected via both interaction fractions after application of netrin-1. As illustrated in Fig. 6, the average M1 increased by 30% and the average M2 by 25% after stimulation with the ligand, consistent with netrin-1-induced colocalization of the two DCC variants.

The detected netrin-1-induced increase in colocalization of full-length DCC with DCC-T-mCherry verifies the capacity of netrin-1 to oligomerize DCC in the absence of a DCC ICD (4). The absence of changes in mean cluster density and degree of aggregation suggests that signaling by the DCC ICD is required to recruit DCC-containing vesicles.

Netrin-1 induces colocalization of DCC and UNC5B with concomitant vesicular DCC recruitment

To further investigate the mechanism underlying netrin-1 signaling by UNC5 homologs and DCC, we cotransfected

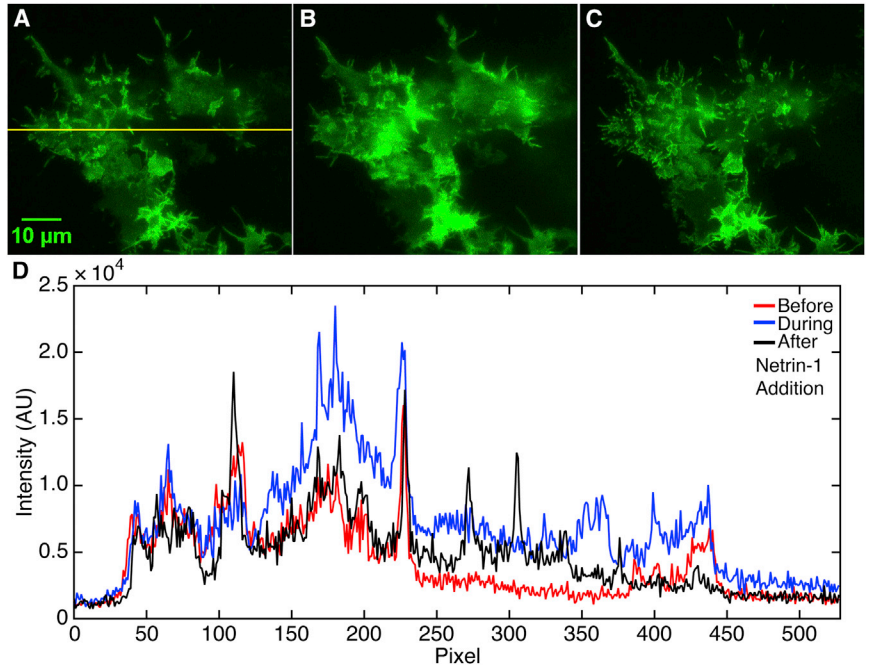

FIGURE 4 TIRF microscopy images from a time series of HEK293T cells, expressing recombinant DCC-EGFP (*A*) Image frame 100 (50 s), before netrin-1 stimulation. (*B*) Image frame 600 (300 s), immediately post-netrin-1 stimulation at ~550 frames. (*C*) Image frame 900 (450 s), showing cells well after netrin-1 stimulation. (*D*) Intensity traces taken from the yellow line at the different times shown from (*A*)–(*C*). The red trace displays the intensity from (*A*) before netrin-1 stimulation. The blue trace displays the intensity from (*B*) immediately after netrin-1 stimulation. The black trace shows the intensity from (*C*) following the redistribution well after netrin-1 stimulation. The single-frame time is 500 ms. To see this figure in color, go online.

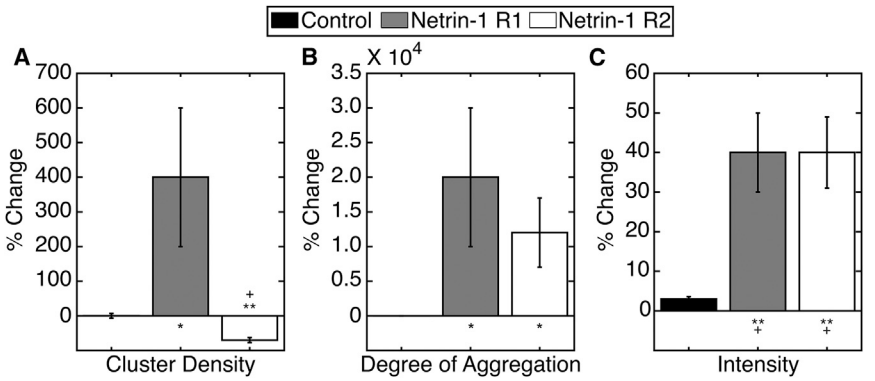

FIGURE 5 Mean percentage changes in (*A*) cluster density, (*B*) degree of aggregation, and (*C*) average intensity measured by TICCS from TIRF images of transfected DCC-EGFP HEK293T cells in the control and netrin-1 stimulation conditions. Error bars indicate the mean ± SE; $*p < 0.05$, $**p < 0.001$ compared to the control, evaluated by one-way ANOVA. Results marked + indicate significance at a 99% CL via a two-tailed *t*-test. $N = 12–21$.

HEK293T cells with both DCC-EGFP and UNC5B-mCherry, performed CLSM imaging with netrin-1 stimulation, and analyzed the image series with TICCS. Average cell population results are depicted in Fig. 7.

The DCC average cluster density increased ~120% after netrin-1 stimulation, whereas the degree of aggregation decreased by ~30%. Colocalization of DCC and UNC5B increased significantly via an ~50% increase in M1. Interestingly, M2 did not increase significantly with M1 in this case. The reason for this can be understood by examining time profiles extracted by TICCS analyses. In some cases, the interaction fractions can be masked due to large changes in total surface population expression. Fig. 8 shows the time series associated with DCC cluster density, degree of aggregation, and M1 colocalization coefficient. Due to the averaging inherent in the TICCS sliding window analysis, the effect of netrin-1 is not precisely localized in time, but the onset of variable change can be perceived.

Maximal colocalization was reached in a minimum of 100 frames after netrin-1 stimulation, with DCC cluster density strongly influencing the change in M1. The degree of DCC aggregation is inversely proportional to cluster density. This observation fits the model where membrane proximal intracellular vesicles within the confocal field of view (more aggregated DCC) deliver DCC to the membrane (less aggregated DCC) after netrin-1 stimulation. This would result in a decrease in the degree of aggregation and an increase in cluster density. Such a mechanism would increase the number of DCC units present, with a concomitant decrease in the aggregation state of those units, similar to what we observed in the singly transfected DCC-EGFP HEK293T cells.

Since M2 is the number of colocalized units normalized by the number of DCC units, a change in M2 is not seen, as the number of colocalized units is constantly proportional to the number of DCC units after netrin-1 stimulation (Fig. 8, *A* and *C*). M1 is reliable, as UNC5B parameter distributions did not change with netrin-1 stimulation. This is consistent with UNC5B units already present in the plasma membrane being recruited into an UNC5B-DCC receptor complex.

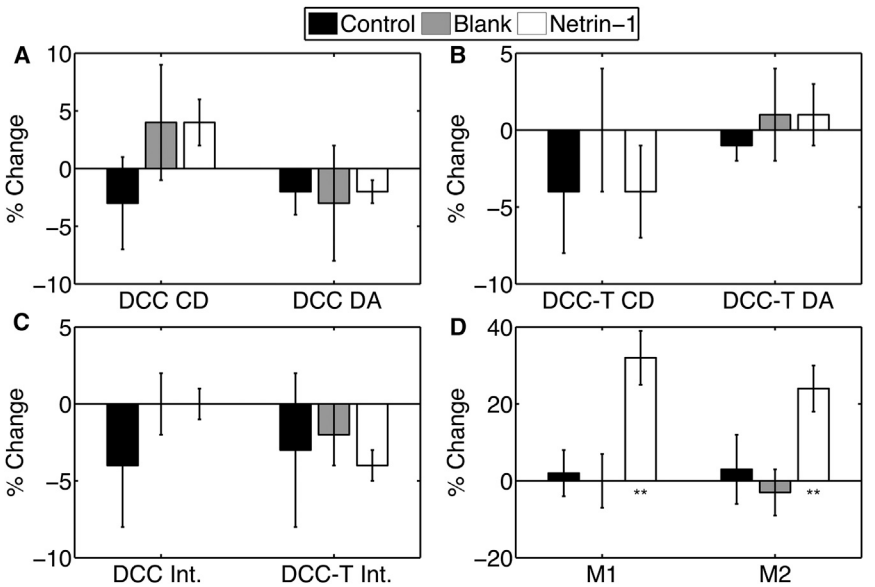

FIGURE 6 Mean percentage changes in cluster density (CD) and degree of aggregation (DA) for DCC-EGFP (*A*) and DCC-T-mCherry (*B*), in the average intensity (Int.) for both DCC variants (*C*), and in the interaction fractions (*D*) in HEK293T cells in the control, blank, and netrin-1 stimulation conditions. Error bars indicate the mean ± SE; $**p < 0.001$ compared to control and blank stimulation, evaluated by one-way ANOVA, and significance at a CL of 99% via a two-tailed *t*-test. $N = 7–17$.

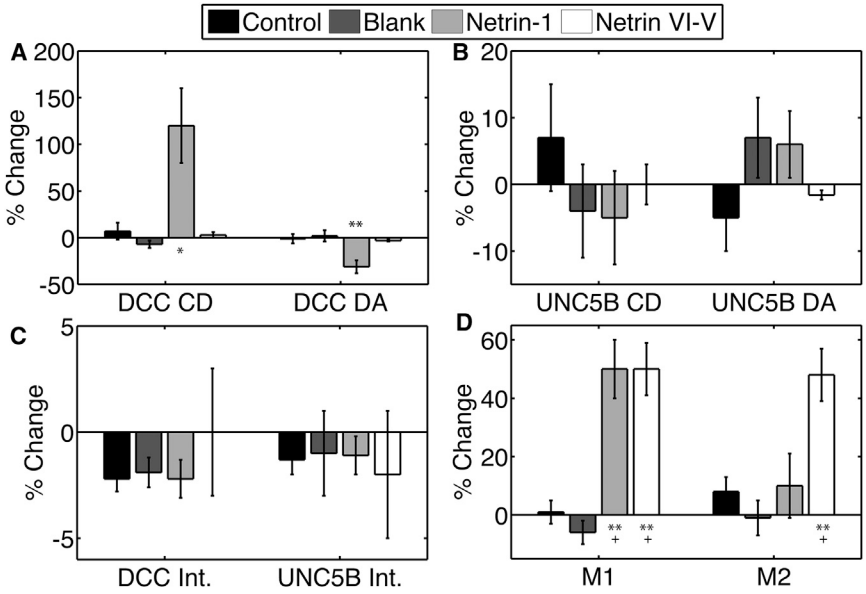

FIGURE 7 Mean percentage changes in cluster density (CD) and degree of aggregation (DA) for DCC-EGFP (*A*) and UNC5B-mCherry (*B*), in the average intensity (Int.) for DCC and UNC5B (*C*), and interaction fractions (*D*), in HEK293T cells in the control, blank, netrin-1, and netrin VI-V stimulation conditions. Error bars indicate the mean ± SE, $*p < 0.05$, $**p < 0.001$ compared to control and blank stimulation, evaluated by one-way ANOVA. All marked results are significant with a paired *t*-test at the 90% CL, whereas + indicates significance at the 99% CL in a two-tailed *t*-test. $N = 15–18$.

M1 decreases after reaching a maximal level, which is due to the simultaneous decrease in DCC cluster density and the slight increase in the degree of aggregation. The reasons behind this reversibility are unclear, but it may correspond to receptor desensitization and endocytosis. For example, netrin-1 binding may cause DCC to dissociate from UNC5B, followed by DCC internalization in vesicles, which remain in the analysis region. Notably, netrin-1 binding activates ligand-mediated downregulation of DCC in neurons by ubiquitination and proteosomal degradation (48), for which endocytosis is required.

Our findings are consistent with netrin-1 stimulation triggering the colocalization of UNC5B and DCC via formation of a receptor complex, with a contribution of DCC recruited from intracellular vesicles to the plasma membrane.

Netrin VI-V induces DCC and UNC5B colocalization, but not DCC recruitment

We next applied the C-terminally truncated netrin VI-V peptide on DCC-EGFP and UNC5B-mCherry transfected cells to determine whether the netrin-1 C-terminal domain is required to induce changes in population distributions similar to those induced by full-length netrin-1. In contrast to treatment with full-length netrin-1, only M1 and M2 increased (each by ~50%) after stimulation with netrin VI-V. This suggests that netrin VI-V does not activate DCC recruitment to the plasma membrane, although it still induces UNC5B and DCC colocalization in the membrane. Together, these findings indicate that the mechanism that recruits plasma membrane DCC is activated by full-length netrin-1, but not by netrin VI-V.

UNC5B and DCC colocalization is not regulated by Src family kinase activation, unlike DCC recruitment

Netrin-1 activation of Src family kinase signaling is an early event downstream of DCC (49,50), but it is unknown whether Src family kinase activation contributes to the formation of a DCC and UNC5B complex and subsequent signaling. To address this, we used cells expressing DCC-EGFP and UNC5B-mCherry, and treated them with the Src family kinase inhibitor PP2 and its inactive analog, PP3 (46) (Fig. 9). After application of netrin-1 and PP2, we observed an increase in colocalization via M1 (90%) and M2 (110%), consistent with formation of the receptor complex. No other changes in population distributions

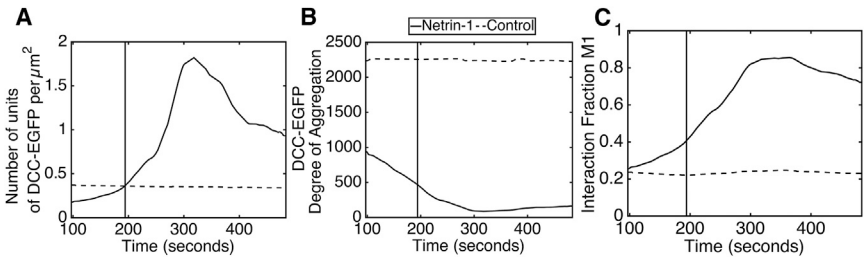

FIGURE 8 Time profiles for cluster density (*A*) and degree of aggregation (*B*) of DCC-EGFP, and for the M1 interaction fraction (*C*) in HEK293T cells coexpressing DCC-EGFP and UNC5B-mCherry in a control experiment (*dotted black line*) and under netrin-1 stimulation (*solid black line*). Netrin-1 stimulation occurs at time frame 200, but due to the averaging nature of the analysis, the effect of netrin-1 is not exact in time. The single-frame time is 0.97 s.

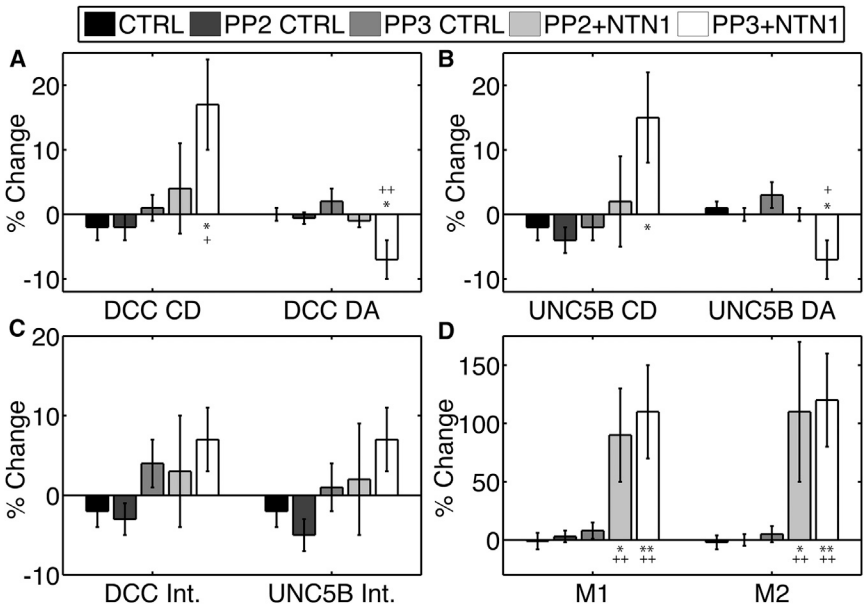

FIGURE 9 Mean percentage change in cluster density (CD) and degree of aggregation (DA) for DCC-EGFP (*A*) and UNC5B-mCherry (*B*), in the average intensity (Int.) for DCC and UNC5B (*C*), and in the interaction fractions (*D*) in HEK293T cells in control, PP2 control, PP3 control, and netrin-1 stimulation in PP2 and PP3. Error bars indicate the mean ± SE; $*p < 0.05$, $**p < 0.001$, evaluated by one-way ANOVA against the relevant control. Results marked + indicate significance with a two-tailed *t*-test at the 90% CL, whereas ++ indicates significance at the 95% CL. $N = 8–12$.

were observed, indicating that Src family kinase inhibition blocked recruitment to the plasma membrane.

The inactive analog, PP3, did not block DCC recruitment by netrin-1, as the DCC average cluster density increased by ~20%, whereas the degree of aggregation decreased by ~7%. In this particular study, population distribution changes in UNC5B were observed with netrin-1 treatment, as the mean cluster density increased by ~20% and the mean degree of aggregation decreased by ~6%. This is consistent with recruitment from membrane proximal intracellular vesicles present within the confocal volume sampled. Colocalization increased, as indicated by increases in both interaction fractions, M1 by ~110% and M2 by ~120%. With PP3, netrin-1 induced the formation of the receptor complex and resulted in plasma membrane recruitment of UNC5B and DCC, whereas the active form, PP2, completely blocked recruitment but not colocalization.

DISCUSSION

DCC and UNC5B direct cell migration during development, with DCC required for chemoattraction and UNC5 homologs required for chemorepulsion in response to netrin-1 (1). Many cells express both DCC and an UNC5 homolog and exhibit the capacity to be attracted or repelled by netrin-1; however, the mechanism by which netrin-1 influences the dynamic distribution of DCC and UNC5 homologs in the plasma membrane remains poorly understood. Here, applying TICCS analysis to confocal and TIRF image series to assess the distribution of DCC and UNC5B, we address the dynamic recruitment, reorganization, and interaction of DCC and UNC5B in living cells in response to netrin-1.

In studies expressing a single receptor, either DCC or UNC5B, our findings are consistent with netrin-1 stimulating DCC recruitment to the plasma membrane from intracellular vesicles docked proximal to the membrane that are within the confocal point-spread function, whereas a more modest increase in plasma membrane UNC5B, in contrast, is recruited from outside of the focal volume. ICS methods have previously been used to study the dynamics and membrane organization of epidermal growth factor receptors, providing evidence for association with membrane microdomains (51). In contrast, in imaging DCC, we observe ICS changes that indicate recruitment to the plasma membrane from an intracellular pool. The results obtained using TIRF microscopy, which reduces detection of cytoplasmic proteins by restricting excitation to a thin optical section within the evanescent field, reinforces this interpretation of the confocal ICS data. Consistent with this, the results of selective biotinylation of cell-surface proteins demonstrate that the addition of netrin-1 triggers a rapid increase in plasma-membrane DCC. A similar increase in cluster density was observed by Rocheleau and Petersen in an ICS study for Sendai viral particle delivery and dispersal in the plasma membrane, although viral entry into the confocal volume originated deeper in the cells in this case, as the mean intensity increased in time as well (52).

In cells expressing both DCC-EGFP and DCC-T-mCherry (lacking the DCC intracellular domain), only an increase in colocalization was detected. This is consistent with netrin-1 cross-linking the extracellular domains of full-length DCC and DCC-T-mCherry, in agreement with recent structural studies (4). In contrast, netrin-1 did not evoke a change in cell-surface levels of DCC when DCC-T-mCherry was coexpressed, suggesting that activation of

intracellular signaling, which requires DCC intracellular domain dimerization is essential for netrin-1-induced recruitment of DCC to the plasma membrane. Consistent with this requirement for activation of intracellular signaling, the Src family kinase inhibitor PP2 also blocked DCC and UNC5B plasma-membrane recruitment, but not receptor-complex formation, after application of netrin-1. These findings support, to our knowledge, a novel mechanism whereby netrin-1 signals to recruit its own receptors to the plasma membrane in a manner dependent on the DCC intracellular domain and Src family kinase signaling.

Recruitment of DCC

In embryonic rat spinal commissural neurons or neocortical neurons, PKA activation causes the recruitment of DCC from an intracellular vesicular pool to the plasma membrane of the growth cone, enhancing axon extension and chemotropic turning to netrin-1 via a mechanism dependent on the v-SNARE VAMP2 (18,53,54). These previous experiments indicate that PKA regulates the sensitivity of embryonic spinal commissural neurons to netrin-1 by modulating DCC trafficking. DCC also forms a complex with the t-SNARE syntaxin-1 and v-SNARE TI-VAMP, and trafficking via these interactions has been implicated in netrin-1-mediated guidance (55,56). Application of netrin-1 itself rapidly increases exocytosis in neuronal growth cones through a mechanism that requires SNARE function and activation of Erk1/2 and Src family kinases (57,58). Although application of netrin-1 alone increases the amount of DCC at the neuronal plasma membrane (54,59), and it has been suggested that recruitment of DCC-containing vesicles may contribute (54,55,59), the specific role of DCC-containing vesicles in this increase is not well understood.

Our findings indicate that DCC expressed in HEK293T cells is recruited from intracellular vesicles to the plasma membrane after stimulation by netrin-1. Application of netrin-1 results in oligomerization of DCC-T-mCherry, indicating that the capacity to signal via the DCC intracellular domain is not essential for oligomerization. In contrast, expression of DCC-T-mCherry negated the netrin-1-induced increase in plasma-membrane DCC, supporting the conclusion that activation of DCC signaling is a prerequisite for the recruitment of DCC-containing vesicles. Interestingly, these findings suggest that DCC activation by netrin-1 may activate a mechanism that locally recruits DCC to the plasma membrane, potentially providing positive feedback to maximize the response to netrin-1.

Extracellularly, netrin-1 binds to the fourth and fifth fibronectin domains of DCC and either Ig domain of UNC5B (1,4). Intracellularly, although the DCC P1 domain promotes heterodimerization by interacting with the UNC5B DB domain (9), our analysis of full-length and DCC-T-mCherry coexpression suggests that the interaction of the DCC and UNC5B intracellular domains is not essential. Instead, netrin-1 cross-linking the DCC extracellular domains appears to be sufficient for oligomerization.

Recruitment of UNC5B

In contrast to DCC, relatively little attention has been paid to the mechanisms and consequences of UNC5 trafficking. Unlike PKA activation promoting DCC recruitment, PKC activation promotes UNC5A endocytosis in neurons, biasing axonal responses from chemorepulsion to chemoattraction in responses to netrin-1 (19,60). Although the mechanism regulating UNC5B intracellular transport is poorly understood, these earlier findings demonstrate that the regulation of UNC5 homolog trafficking can have critical functional consequences. Our current findings demonstrate netrin-1-induced UNC5B recruitment to the plasma membrane, with and without coexpression of DCC, revealing, to our knowledge, a novel mechanism regulating the trafficking and distribution of UNC5B.

Regulation of UNC5B-DCC complexes

Genetic studies in *Drosophila* have provided evidence that coexpression of DCC and an UNC5 homolog increase sensitivity to netrin-1 and argue that a DCC-UNC5 homolog receptor complex facilitates long-range chemorepulsion (11). Here, we directly visualize the formation of an UNC5B-DCC complex in living cells in real time and monitor the recruitment of both receptors to the plasma membrane by netrin-1.

Although the netrin-1 VI-V peptide does not function as a chemoattractant for commissural neurons, it is sufficient to repel migrating oligodendrocyte precursor cells (17), suggesting that it activates UNC5 homolog function. Here, we present evidence that netrin-1 VI-V triggers UNC5B-DCC multimerization, similar to full-length netrin-1; however, the netrin-1 VI-V peptide does not activate receptor recruitment to the plasma membrane, consistent with an inability to activate DCC and the absence of chemoattractant activity.

Inhibiting Src family kinase activation, a key signaling mechanism downstream of DCC, similarly did not block netrin-1-induced UNC5B-DCC multimerization, but disrupted receptor recruitment to the plasma membrane. Together with the results obtained using netrin-1 VI-V, truncated DCC-T-mCherry, and Src family kinase inhibition, these findings suggest a novel role for netrin-1 activation of DCC signaling in the recruitment of netrin receptors to the plasma membrane.

CONCLUSIONS

Using sliding-window TICCS, we have investigated the influence of netrin-1 on the distribution of DCC and UNC5B in living cells. Our findings reveal that DCC and UNC5B are recruited to the plasma membrane by netrin-1, with DCC

recruited from intracellular vesicles within the local ROI. Furthermore, we detect the formation of an UNC5B and DCC complex triggered by netrin-1, with concomitant recruitment of DCC to the plasma membrane. Studies that utilize DCC lacking an ICD, the netrin-1 VI-V peptide, and pharmacological inhibition of Src family kinase signaling support the conclusion that DCC and UNC5B recruitment to the plasma membrane requires DCC signaling, whereas DCC-DCC or DCC-UNC5B multimerization by netrin-1 does not. Time profiles analyzed in each condition reveal details of population dynamics and colocalization that indicate the rapid formation of receptor complexes, maximal within 100 s after netrin-1 application, with the recruitment response on a similar timescale.

Uncovering the molecular mechanisms involved in netrin receptor trafficking will provide a deeper understanding of the regulation of neural circuit formation and potentially identify new molecular targets to promote functional recovery after injury or neurodegeneration.

SUPPORTING MATERIAL

Supporting Materials and Methods, Supporting Results, and six figures are available at http://www.biophysj.org/biophysj/supplemental/S0006-3495(15)04765-7.

AUTHOR CONTRIBUTIONS

B.R., I.B.M., and P.D.D. designed and performed the preliminary colocalization experiments for the UNC5B/DCC system. A.A.G. designed and performed the research, provided analysis codes, analyzed the data, and wrote the article. V.R. built the homemade TIRF microscope system. R.J.M. performed the PP2/PP3 experiments and aided in the data analysis. I.V.B. performed the cell surface biotinylation experiment and Western blot analysis. T.E.K. and P.W.W. designed the research and wrote the article.

ACKNOWLEDGMENTS

Confocal microscopy for this work was performed in the McGill University Life Sciences Complex Advanced BioImaging Facility (ABIF). Purchase of equipment in the facility was made possible with funding from the Canadian Foundation for Innovation (CFI) and the Ministère du Développement économique, innovation et exportation Québec (MDEIE). We acknowledge Alexei Kazarine for help in interfacing the homemade TIRF microscope system.

This work was supported by operating grants from the Natural Sciences and Engineering Research Council of Canada (NSERC) to P.W.W. and from the Canadian Institute of Health Research (CIHR) to T.E.K. A.A.G. was a recipient of the NSERC-CREATE Bionanomachines Program scholarship and is supported by the NSERC-CREATE Neuroengineering Program. B.R. acknowledges financial support from Swiss National Science Foundation fellowship no. PA00P3-131496 and the CREATE Neuroengineering Program. V.R. acknowledges financial support from the CREATE Bionanomachines Program. R.J.M. was a recipient of an NSERC URSA scholarship. I.V.B. was supported by an NSERC Alexander Graham Bell Canada Graduate scholarship. T.E.K. was supported by a scholarship from the Killam Trust and a Chercheur Nationaux Award from the Fonds de la Recherche en Santé du Québec.

REFERENCES

1. Lai Wing Sun, K., J. P. Correia, and T. E. Kennedy. 2011. Netrins: versatile extracellular cues with diverse functions. *Development.* 138:2153–2169.
2. Yurchenco, P. D., and W. G. Wadsworth. 2004. Assembly and tissue functions of early embryonic laminins and netrins. *Curr. Opin. Cell Biol.* 16:572–579.
3. Keino-Masu, K., M. Masu, …, M. Tessier-Lavigne. 1996. Deleted in Colorectal Cancer (DCC) encodes a netrin receptor. *Cell.* 87:175–185.
4. Xu, K., Z. Wu, …, D. B. Nikolov. 2014. Neural migration. Structures of netrin-1 bound to two receptors provide insight into its axon guidance mechanism. *Science.* 344:1275–1279.
5. Geisbrecht, B. V., K. A. Dowd, …, D. J. Leahy. 2003. Netrin binds discrete subdomains of DCC and UNC5 and mediates interactions between DCC and heparin. *J. Biol. Chem.* 278:32561–32568.
6. Stein, E., Y. Zou, …, M. Tessier-Lavigne. 2001. Binding of DCC by netrin-1 to mediate axon guidance independent of adenosine A2B receptor activation. *Science.* 291:1976–1982.
7. Leonardo, E. D., L. Hinck, …, M. Tessier-Lavigne. 1997. Vertebrate homologues of *C. elegans* UNC-5 are candidate netrin receptors. *Nature.* 386:833–838.
8. Hofmann, K., and J. Tschopp. 1995. The death domain motif found in Fas (Apo-1) and TNF receptor is present in proteins involved in apoptosis and axonal guidance. *FEBS Lett.* 371:321–323.
9. Hong, K., L. Hinck, …, E. Stein. 1999. A ligand-gated association between cytoplasmic domains of UNC5 and DCC family receptors converts netrin-induced growth cone attraction to repulsion. *Cell.* 97:927–941.
10. Colavita, A., and J. G. Culotti. 1998. Suppressors of ectopic UNC-5 growth cone steering identify eight genes involved in axon guidance in *Caenorhabditis elegans*. *Dev. Biol.* 194:72–85.
11. Keleman, K., and B. J. Dickson. 2001. Short- and long-range repulsion by the *Drosophila* Unc5 netrin receptor. *Neuron.* 32:605–617.
12. Macabenta, F. D., A. G. Jensen, …, S. G. Kramer. 2013. Frazzled/DCC facilitates cardiac cell outgrowth and attachment during *Drosophila* dorsal vessel formation. *Dev. Biol.* 380:233–242.
13. Serafini, T., T. E. Kennedy, …, M. Tessier-Lavigne. 1994. The netrins define a family of axon outgrowth-promoting proteins homologous to *C. elegans* UNC-6. *Cell.* 78:409–424.
14. Wang, H., N. G. Copeland, …, M. Tessier-Lavigne. 1999. Netrin-3, a mouse homolog of human NTN2L, is highly expressed in sensory ganglia and shows differential binding to netrin receptors. *J. Neurosci.* 19:4938–4947.
15. Bányai, L., and L. Patthy. 1999. The NTR module: domains of netrins, secreted frizzled related proteins, and type I procollagen C-proteinase enhancer protein are homologous with tissue inhibitors of metalloproteases. *Protein Sci.* 8:1636–1642.
16. Kappler, J., S. Franken, …, K. W. Koch. 2000. Glycosaminoglycan-binding properties and secondary structure of the C-terminus of netrin-1. *Biochem. Biophys. Res. Commun.* 271:287–291.
17. Bin, J. M., S. Rajasekharan, …, T. E. Kennedy. 2013. Full-length and fragmented netrin-1 in multiple sclerosis plaques are inhibitors of oligodendrocyte precursor cell migration. *Am. J. Pathol.* 183:673–680.
18. Moore, S. W., and T. E. Kennedy. 2006. Protein kinase A regulates the sensitivity of spinal commissural axon turning to netrin-1 but does not switch between chemoattraction and chemorepulsion. *J. Neurosci.* 26:2419–2423.
19. Bartoe, J. L., W. L. McKenna, …, L. Hinck. 2006. Protein interacting with C-kinase 1/protein kinase Cα-mediated endocytosis converts netrin-1-mediated repulsion to attraction. *J. Neurosci.* 26:3192–3205.
20. Magde, D., W. W. Webb, and E. Elson. 1972. Thermodynamic fluctuations in a reacting system—measurement by fluorescence correlation spectroscopy. *Phys. Rev. Lett.* 29:705–708.
21. Elson, E. L., and D. Magde. 1974. Fluorescence correlation spectroscopy. I. Conceptual basis and theory. *Biopolymers.* 13:1–27.

22. Magde, D., E. L. Elson, and W. W. Webb. 1974. Fluorescence correlation spectroscopy. II. An experimental realization. *Biopolymers.* 13:29–61.

23. Eigen, M., and R. Rigler. 1994. Sorting single molecules: application to diagnostics and evolutionary biotechnology. *Proc. Natl. Acad. Sci. USA.* 91:5740–5747.

24. Schwille, P., F. J. Meyer-Almes, and R. Rigler. 1997. Dual-color fluorescence cross-correlation spectroscopy for multicomponent diffusional analysis in solution. *Biophys. J.* 72:1878–1886.

25. Haustein, E., and P. Schwille. 2007. Fluorescence correlation spectroscopy: novel variations of an established technique. *Annu. Rev. Biophys. Biomol. Struct.* 36:151–169.

26. Weidemann, T., and P. Schwille. 2009. Fluorescence correlation spectroscopy in living cells. *In* Handbook of Single-Molecule Biophysics. Springer-Verlag, New York, pp. 217–241.

27. Petersen, N. O., P. L. Höddelius, …, K. E. Magnusson. 1993. Quantitation of membrane receptor distributions by image correlation spectroscopy: concept and application. *Biophys. J.* 65:1135–1146.

28. Wiseman, P. W., and N. O. Petersen. 1999. Image correlation spectroscopy. II. Optimization for ultrasensitive detection of preexisting platelet-derived growth factor-β receptor oligomers on intact cells. *Biophys. J.* 76:963–977.

29. Wiseman, P. W., J. A. Squier, …, K. R. Wilson. 2000. Two-photon image correlation spectroscopy and image cross-correlation spectroscopy. *J. Microsc.* 200:14–25.

30. Srivastava, M., and N. O. Petersen. 1996. Image cross-correlation spectroscopy: a new experimental biophysical approach to measurement of slow diffusion of fluorescent molecules. *Methods Cell Sci.* 18:47–54.

31. Digman, M. A., C. M. Brown, …, E. Gratton. 2005. Measuring fast dynamics in solutions and cells with a laser scanning microscope. *Biophys. J.* 89:1317–1327.

32. Digman, M. A., P. Sengupta, …, E. Gratton. 2005. Fluctuation correlation spectroscopy with a laser-scanning microscope: exploiting the hidden time structure. *Biophys. J.* 88:L33–L36.

33. Comeau, J. W. D., S. Costantino, and P. W. Wiseman. 2006. A guide to accurate fluorescence microscopy colocalization measurements. *Biophys. J.* 91:4611–4622.

34. Guo, S. M., N. Bag, …, M. Bathe. 2014. Bayesian total internal reflection fluorescence correlation spectroscopy reveals hIAPP-induced plasma membrane domain organization in live cells. *Biophys. J.* 106:190–200.

35. Ries, J., E. P. Petrov, and P. Schwille. 2008. Total internal reflection fluorescence correlation spectroscopy: effects of lateral diffusion and surface-generated fluorescence. *Biophys. J.* 95:390–399.

36. Ciccotosto, G. D., N. Kozer, …, A. H. Clayton. 2013. Aggregation distributions on cells determined by photobleaching image correlation spectroscopy. *Biophys. J.* 104:1056–1064.

37. Hebert, B., S. Costantino, and P. W. Wiseman. 2005. Spatiotemporal image correlation spectroscopy (STICS) theory, verification, and application to protein velocity mapping in living CHO cells. *Biophys. J.* 88:3601–3614.

38. Brown, C. M., B. Hebert, …, P. W. Wiseman. 2006. Probing the integrin-actin linkage using high-resolution protein velocity mapping. *J. Cell Sci.* 119:5204–5214.

39. Toplak, T., E. Pandzic, …, P. W. Wiseman. 2012. STICCS reveals matrix-dependent adhesion slipping and gripping in migrating cells. *Biophys. J.* 103:1672–1682.

40. Di Rienzo, C., E. Gratton, …, F. Cardarelli. 2013. Fast spatiotemporal correlation spectroscopy to determine protein lateral diffusion laws in live cell membranes. *Proc. Natl. Acad. Sci. USA.* 110:12307–12312.

41. Kennedy, T. E., H. Wang, …, M. Tessier-Lavigne. 2006. Axon guidance by diffusible chemoattractants: a gradient of netrin protein in the developing spinal cord. *J. Neurosci.* 26:8866–8874.

42. Comeau, J. W. D., D. L. Kolin, and P. W. Wiseman. 2008. Accurate measurements of protein interactions in cells via improved spatial image cross-correlation spectroscopy. *Mol. Biosyst.* 4:672–685.

43. Costantino, S., J. W. D. Comeau, …, P. W. Wiseman. 2005. Accuracy and dynamic range of spatial image correlation and cross-correlation spectroscopy. *Biophys. J.* 89:1251–1260.

44. Wiseman, P. W., C. M. Brown, …, A. F. Horwitz. 2004. Spatial mapping of integrin interactions and dynamics during cell migration by image correlation microscopy. *J. Cell Sci.* 117:5521–5534.

45. Kolin, D. L., S. Costantino, and P. W. Wiseman. 2006. Sampling effects, noise, and photobleaching in temporal image correlation spectroscopy. *Biophys. J.* 90:628–639.

46. Hanke, J. H., J. P. Gardner, …, P. A. Connelly. 1996. Discovery of a novel, potent, and Src family-selective tyrosine kinase inhibitor. Study of Lck- and FynT-dependent T cell activation. *J. Biol. Chem.* 271:695–701.

47. Shekarabi, M., and T. E. Kennedy. 2002. The netrin-1 receptor DCC promotes filopodia formation and cell spreading by activating Cdc42 and Rac1. *Mol. Cell. Neurosci.* 19:1–17.

48. Kim, T. H., H. K. Lee, …, H. T. Park. 2005. Netrin induces down-regulation of its receptor, Deleted in Colorectal Cancer, through the ubiquitin-proteasome pathway in the embryonic cortical neuron. *J. Neurochem.* 95:1–8.

49. Li, W., J. Lee, …, K. L. Guan. 2004. Activation of FAK and Src are receptor-proximal events required for netrin signaling. *Nat. Neurosci.* 7:1213–1221.

50. Meriane, M., J. Tcherkezian, …, N. Lamarche-Vane. 2004. Phosphorylation of DCC by Fyn mediates Netrin-1 signaling in growth cone guidance. *J. Cell Biol.* 167:687–698.

51. Keating, E., A. Nohe, and N. O. Petersen. 2008. Studies of distribution, location and dynamic properties of EGFR on the cell surface measured by image correlation spectroscopy. *Eur. Biophys. J.* 37:469–481.

52. Rocheleau, J. V., and N. O. Petersen. 2001. The Sendai virus membrane fusion mechanism studied using image correlation spectroscopy. *Eur. J. Biochem.* 268:2924–2930.

53. Bouchard, J.-F., K. E. Horn, …, T. E. Kennedy. 2008. Depolarization recruits DCC to the plasma membrane of embryonic cortical neurons and enhances axon extension in response to netrin-1. *J. Neurochem.* 107:398–417.

54. Bouchard, J.-F., S. W. Moore, …, T. E. Kennedy. 2004. Protein kinase A activation promotes plasma membrane insertion of DCC from an intracellular pool: a novel mechanism regulating commissural axon extension. *J. Neurosci.* 24:3040–3050.

55. Cotrufo, T., R. M. Andrés, …, E. Soriano. 2012. Syntaxin 1 is required for DCC/Netrin-1-dependent chemoattraction of migrating neurons from the lower rhombic lip. *Eur. J. Neurosci.* 36:3152–3164.

56. Cotrufo, T., F. Pérez-Brangulí, …, E. Soriano. 2011. A signaling mechanism coupling netrin-1/deleted in colorectal cancer chemoattraction to SNARE-mediated exocytosis in axonal growth cones. *J. Neurosci.* 31:14463–14480.

57. Ros, O., T. Cotrufo, …, E. Soriano. 2015. Regulation of patterned dynamics of local exocytosis in growth cones by netrin-1. *J. Neurosci.* 35:5156–5170.

58. Winkle, C. C., L. M. McClain, …, S. L. Gupton. 2014. A novel Netrin-1-sensitive mechanism promotes local SNARE-mediated exocytosis during axon branching. *J. Cell Biol.* 205:217–232.

59. Matsumoto, H., and M. Nagashima. 2010. Netrin-1 elevates the level and induces cluster formation of its receptor DCC at the surface of cortical axon shafts in an exocytosis-dependent manner. *Neurosci. Res.* 67:99–107.

60. McKenna, W. L., C. Wong-Staal, …, J. L. Bartoe. 2008. Netrin-1-independent adenosine A2b receptor activation regulates the response of axons to netrin-1 by controlling cell surface levels of UNC5A receptors. *J. Neurochem.* 104:1081–1090.